Title
Passive plasmonic nanoantenna arrays for high-efficiency optical-to-terahertz conversion

Author
Parimi, Vivek

Publication Date
2022

Peer reviewed|Thesis/dissertation

UNIVERSITY OF CALIFORNIA

Los Angeles

Passive plasmonic nanoantenna arrays for high-efficiency optical-to-terahertz conversion

A thesis submitted in partial satisfaction

of the requirements for the degree Master of Science

in Electrical & Computer Engineering

by

Vivek Parimi

2022

ABSTRACT OF THE THESIS

Passive plasmonic nanoantenna arrays for high-efficiency optical-to-terahertz conversion

by

Vivek Parimi

Master of Science in Electrical & Computer Engineering

University of California, Los Angeles, 2022

Professor Mona Jarrahi, Chair

Photoconductive antennas are extensively used for the generation of terahertz radiation. They generally consist of an antenna fabricated on a photo-absorbing semiconductor substrate. When illuminated by an optical pump beam with terahertz frequency components, photocarriers are generated in the substrate. The photogenerated carriers drift to the antenna under an external bias voltage to induce a terahertz photocurrent that drives the antenna to generate terahertz radiation.

One of the major limitations of existing photoconductive antennas, especially those operating at telecommunication optical wavelengths (~1550 nm), is their large dark current level, which degrades device reliability due to excessive Joule heating. To address this limitation, a new class of bias-free terahertz emitters was recently introduced, which utilizes the naturally induced built-in electric field at the surface of semiconductors to drift the photo-generated carriers. By eliminating the bias voltage and dark current, a highly reliable optical-to-terahertz conversion is achieved.

The first generation of these bias-free terahertz emitters utilized an array of plasmonic nanoantennas in the form of gratings fabricated on epitaxially-grown undoped and p^+ doped InAs layers on a semi-insulating GaAs substrate. Using this bias-free terahertz emitter, record-high optical-to-terahertz conversion efficiencies were achieved compared to other bias-free terahertz emitters based on nonlinear optical process, photo-Dember effect, and spintronics. Despite its superior efficiency compared to the state-of-the art, the optical-to-terahertz conversion efficiency of this emitter is limited by leakage of the terahertz current from the terahertz radiating elements to the highly doped substrate and destructive interference of the photocurrent components injected to the terahertz radiating elements. This research is focused on the design and optimization of a new generation of plasmonic nanoantenna arrays to address these efficiency limitations and further enhance the optical-terahertz conversion efficiency of bias-free terahertz emitters.

The thesis of Vivek Parimi is approved

Benjamin S. Williams

Aydin Babakhani

Yuanxun Wang

Mona Jarrahi, Committee Chair

University of California, Los Angeles

2022

To my family and friends

Table of Contents

Chapter 1: Introduction 1

1.1 Introduction to Terahertz Technology 1

1.2 Photoconductive THz sources 2

1.3 Bias-free photoconductive THz sources 4

Chapter 2: Nanoantenna array design 9

2.1 Nanoantenna array design parameters 9

2.2 Circuit model of the nanoantenna array 12

Chapter 3: Design optimization 15

3.1 Design optimization strategy 15

3.2 THz Simulations 17

3.3 Material properties at THz frequencies 17

3.4 THz leakage current simulations 18

3.5 Optical simulations 25

3.6 Optical absorption optimization 26

3.7 Nanoantenna radiation resistance 28

3.8 Antenna array factor 28

3.9 Optimum design 29

Chapter 4: Conclusions and Future Work 31

References 32

List of Figures

Figure 1.1: Schematic diagram of the nanoantenna array designed to couple the optically excited surface plasmon waves to the surface states, where the photo-generated electrons are drifted to the nanoantenna array to generate THz radiation [21]. 5

Figure 1.2: a) Band diagram of a p-doped InAs layer at different p-type doping concentrations are shown in white. The color map shows the strength of the built-in electric field. b) The measured THz radiation spectra from identical nanoantenna arrays fabricated on three InAs substrates with p-type doping concentrations of 10^{17}, 10^{18}, and 10^{19} cm^{-3} in response to the same optical pump beam. The radiation spectra are shown in a linear scale to clearly show the wavelength conversion efficiency increases at higher p-type doping concentrations. c) Band diagram and the built-in electric field profiles when an undoped InAs layer is incorporated between the p-doped InAs epilayer and the Ti/Au contact. d) The measured THz radiation spectra from identical nanoantenna arrays fabricated on four InAs substrates with undoped InAs layer thicknesses of 0, 100, 200, and 350 nm grown on an InAs epilayer with a p-type doping of 10^{19} cm^{-3}, indicating that the highest wavelength conversion efficiency is achieved for a 100 nm thick undoped InAs layer, which provides the highest spatial overlap between the built-in electric field and photo-generated carrier profile [21]. 7

Figure 2.1: Geometric parameters of a triangular nanoantenna element 9

Figure 2.2: Schematic of a single nanoantenna with the p^+ doped InAs layer being partially etched. The unetched section of the p^+ doped InAs is shown in purple. 11

Figure 2.3: The nanoantenna array is modeled as a parallel RC circuit with an antenna capacitance (C_a), a substrate capacitance (C_s) and a substrate resistance (R_s). The periodicity of the nanoantenna array in the x and y directions are given by p_x and p_y, respectively. 12

Figure 3.1: The band structure of the undoped InAs layer (0-0.1um) followed by the p^+ doped InAs layer (0.1-0.6 um) and the SI-GaAs substrate (0.6-0.8 um). 18

Figure 3.2: Variation of the THz leakage current with t_{etch} 19

Figure 3.3: Variation of the THz leakage current with the periodicity of the nanoantenna 20

Figure 3.4: The variation of the THz leakage current when changing only p_y or p_x, while keeping the other periodicity fixed at 1000 nm. 21

Figure 3.5: Variation of the THz leakage current as a function of the operation frequency. 22

Figure 3.6: Variation of the THz leakage current as a function of the nanoantenna size, a..... 23

Figure 3.7: Variation of the THz leakage current as a function of the nanoantenna contact area with the undoped InAs layer, b. 24

Figure 3.8: Variation of the THz leakage current as a function of the nanoantenna triangular angle. 25

Figure 3.9: Optical absorption profile for three different metal thicknesses, t_{Au}, while t_{ins} is fixed at 20 nm..... 27

Figure 3.10: The absorption of a 1550 nm optical beam in the undoped InAs layer under the nanoantenna contact (P_{abs}) as a function of the nanoantenna dimensions for a 500 nm periodicity in the x and y directions. 27

List of Tables

Table 1: Design parameters of the optimized nanoantenna array structure 30

ACKNOWLEDGEMENTS

I would like to thank my advisor, Professor Mona Jarrahi, for her guidance and support in this project. I would also like to thank Deniz Turan, Ping Keng Lu, Xurong Li, Joseph Hwang, and Tianyi Gan, and for their help during this research. I would also like to thank my family for their support.

Chapter 1: Introduction

1.1 Introduction to Terahertz Technology

The terahertz (THz) regime has long been an untapped part of the electromagnetic (EM) spectrum. It is located between the radio frequency (RF) and infrared ranges and is loosely defined as the region covering frequencies between 0.1 THz and 10 THz. This range was historically referred to as the THz gap since technology to detect or generate THz radiation was very inefficient for scientific or industrial applications. This is because the highest operation frequency of conventional electronic devices is limited by the cutoff frequency of transistors and device parasitics, while the longest operation wavelength of conventional optical devices is limited by the bandgap energy of semiconductors.

With the advancement of THz technology over decades, numerous types of devices have been developed for high efficiency THz generation. Some of the earliest THz sources were based on blackbody radiation such as the mercury lamp [1] and the globar [2,3]. By the 1970s, several research groups were able to develop non-linear crystal based far infrared sources that reached the upper limits of the THz regime. Vacuum electronic based sources such as backward-wave oscillators [4,5], gyrotrons [6,7], synchrotrons [8,9] and free electron lasers [10,11] were also developed over time. Solid state electronics also caught up with other technologies as Gunn diodes [12] were developed. The previous generations of devices had their fair share of disadvantages such as bulky designs, low power output, and low efficiency.

In recent times, quantum cascade lasers (QCLs) have proven to be a successful technology in generation of high-power THz radiation [13]. However, THz-QCls require cryogenic cooling, which may be considered undesirable for some applications. The use of nonlinear optical processes [14] also shows great promise to generate high-power and broadband THz radiation through optical frequency down-conversion to THz frequencies. However, these nonlinear processes have theoretical efficiency limitations known as the Manley-Rowe limit [15]

1.2 Photoconductive THz sources

The use of photoconductive sources for THz generation was first demonstrated in 1984 [16] and since then the technology has advanced extensively. A typical photoconductive source consists of a material with sub-picosecond recombination time which is driven by an optical pump and a radiating element or antenna to efficiently radiate the generated THz currents. These devices can be used either in pulsed operation or continuous-wave operation.

In pulsed operation, a sub-picosecond optical beam is incident on the photoconductive material. The photons in this beam are absorbed in the photoconductor and electron-hole pairs are generated. An external bias voltage is applied to drift these electrons and holes to the antenna electrodes which results in the generation of a THz photocurrent. This photocurrent drives the antenna to generate THz radiation.

In CW operation, the photoconductive material is excited using a pair of optical beams that have a frequency difference corresponding to a THz frequency. Concentration of the electron-hole pairs excited by these optical beams and the resulting photocurrent has the same THz frequency as the difference in the frequency of the two optical beams. An external bias is applied to the

photoconductor to induce a THz photocurrent to drive the antenna and generate radiation at the same THz frequency.

Conventional photoconductive sources have low quantum efficiency due to multiple reasons. Due to the ultrafast nature of the THz generation process, only a fraction of the carriers generated end up contributing to the THz radiation. This is because carriers that are excited further away from the electrodes do not drift to the electrodes in time before recombination takes place. This is a byproduct of the sub-picosecond lifetime of carriers in the photoconductive materials used. Materials with such a short carrier lifetime tend to have low mobilities as well, which further reduces the number of carriers that reach the electrodes.

Previous research [17-20] has shown that by the use of plasmonic contact electrodes, the quantum efficiency of photoconductive THz sources can be greatly improved. The incident optical beam is focused on the plasmonic contact electrodes such that a surface plasmon wave is excited at the interface between the metal contact and the photoconductive substrate. This increases the intensity of the optical energy near the electrodes and subsequently the number of the photogenerated carrier in close vicinity to these electrodes. This reduces the average transport length of carriers to reach the electrodes to drive the antenna with a THz photocurrent. Photoconductive THz sources utilizing plasmonic contact electrodes have provided several orders of magnitude higher efficiencies and radiation powers compared to their non-plasmonic counterparts [20].

Despite the efficiency enhancement offered by plasmonic photoconductive THz sources, the reliability of photoconductive THz sources is still limited by their dark current. Especially, at 1550 nm optical wavelengths at which high-performance, compact, and cost-efficient pump sources are

commercially available, the relatively low resistivity of the photo-absorbing photoconductors results in high dark currents, which can lead to thermal breakdown before reaching high THz powers. In order to mitigate these drawbacks, a bias-free plasmonic photoconductive source was recently developed, which totally eliminates the dark current, leading to highly reliable and efficient THz generation [21].

1.3 Bias-free photoconductive THz sources

The first-generation bias-free photoconductive source [21] enables passive optical-to-THz wavelength conversion by using a naturally induced built-in electric field in InAs. This built-in electric field is induced because the maxima of the surface state electron density is located above the bandgap of InAs. This causes the photo-generated electrons to move towards the bulk of the InAs, especially when the bulk InAs is highly p-type doped, and results in the generation of a massive built-in electric field. An external optical beam at ~1550 nm wavelength is used to generate electrons and accelerate them through this electric field towards a nanoantenna array to generate THz radiation. The nanoantenna array, which is in the form of gratings, was designed to excite surface plasmon waves to efficiently generate electrons in close vicinity to the metal-InAs interface to obtain a high spatial overlap between the electron density and the built-in electric field strength, as shown in Figure 1.1.

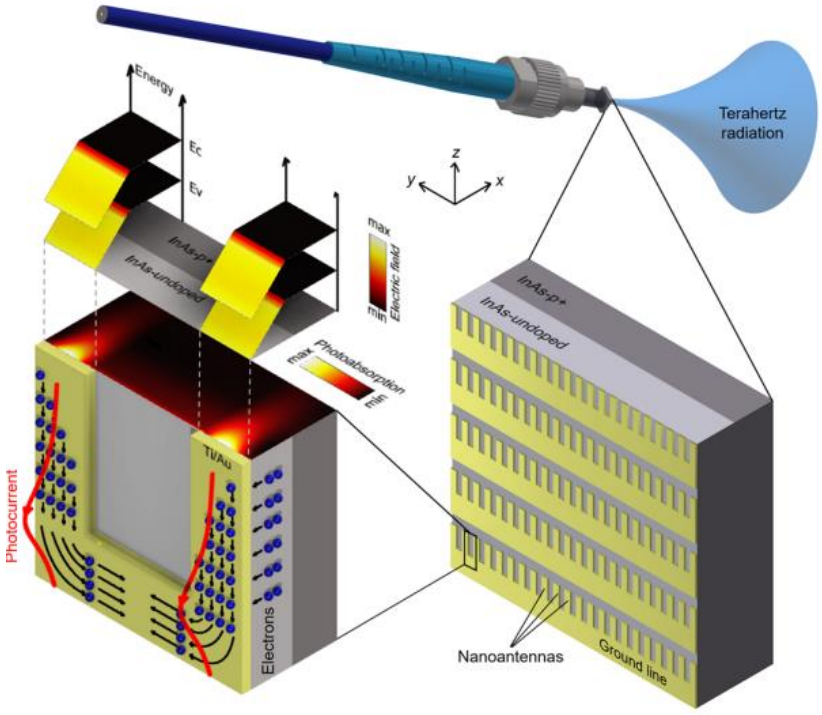

Figure 1.1: Schematic diagram of the nanoantenna array designed to couple the optically excited surface plasmon waves to the surface states, where the photo-generated electrons are drifted to the nanoantenna array to generate THz radiation [21].

Previous studies on this bias-free photoconductive THz generation method also investigated the impact of the semiconductor structure on the band bending and, thus, the strength of the built-in electric field. It was shown that band-engineering would be possible by varying the thickness of the InAs substrate layers as well as their doping concentration, as shown in Figure 1.2. The optimum design was obtained by finding the maximum spatial overlap between the built-in field and the photo-absorption profile for different substrate structures. This optimum design was able to provide passive optical-to-THz conversion with 4 orders of magnitude higher efficiencies than the nonlinear optical processes [21].

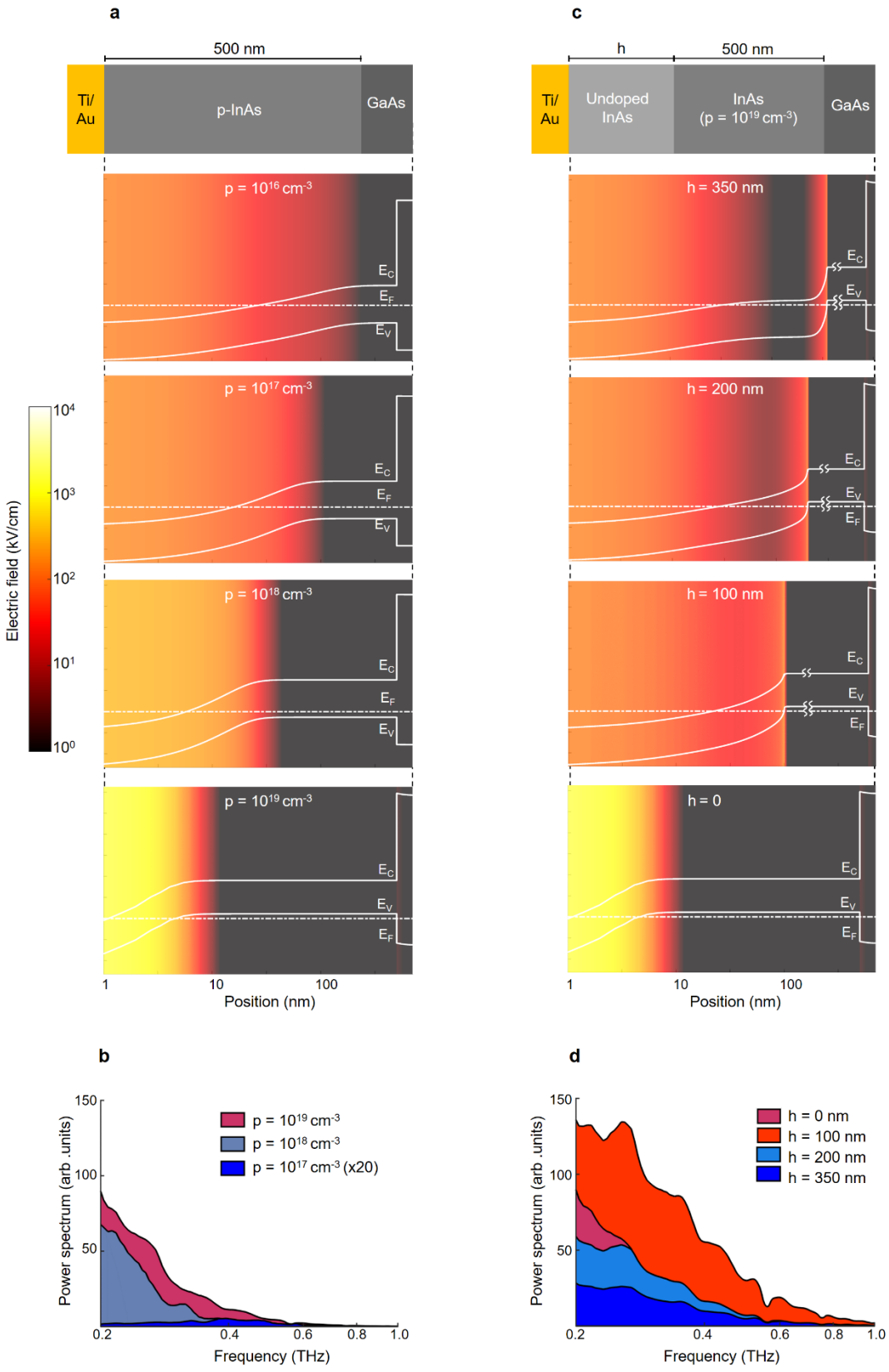
a
500 nm
Ti/ Au
p-InAs
GaAs
p = 10^16 cm^-3
p = 10^17 cm^-3
p = 10^18 cm^-3
p = 10^19 cm^-3
E_C
E_F
E_V
Electric field (kV/cm)
10^4
10^3
10^2
10^1
10^0
1
10
100
Position (nm)
c
h
500 nm
Ti/ Au
Undoped InAs
InAs (p = 10^19 cm^-3)
GaAs
h = 350 nm
h = 200 nm
h = 100 nm
h = 0
b
Power spectrum (arb .units)
150
100
50
p = 10^19 cm^-3
p = 10^18 cm^-3
p = 10^17 cm^-3 (x20)
0.2
0.4
0.6
0.8
1.0
Frequency (THz)
d
h = 0 nm
h = 100 nm
h = 200 nm
h = 350 nm

Figure 1.2: a) Band diagram of a p-doped InAs layer at different p-type doping concentrations are shown in white. The color map shows the strength of the built-in electric field. b) The measured THz radiation spectra from identical nanoantenna arrays fabricated on three InAs substrates with p-type doping concentrations of 10^{17}, 10^{18}, and 10^{19} cm^{-3} in response to the same optical pump beam. The radiation spectra are shown in a linear scale to clearly show the wavelength conversion efficiency increases at higher p-type doping concentrations. c) Band diagram and the built-in electric field profiles when an undoped InAs layer is incorporated between the p-doped InAs epilayer and the Ti/Au contact. d) The measured THz radiation spectra from identical nanoantenna arrays fabricated on four InAs substrates with undoped InAs layer thicknesses of 0, 100, 200, and 350 nm grown on an InAs epilayer with a p-type doping of 10^{19} cm^{-3}, indicating that the highest wavelength conversion efficiency is achieved for a 100 nm thick undoped InAs layer, which provides the highest spatial overlap between the built-in electric field and photo-generated carrier profile [21].

Despite the great promise of the first-generation bias-free photoconductive THz source, there are multiple limitations that should be addressed to further enhance its optical-to-THz conversion efficiency.

First, since the carriers are generated along the entire length of the nanoantennas, the injected photocurrent to the nanoantennas can flow in both directions, forming standing waves on the nanoantennas and reducing the overall radiation efficiency. In order to mitigate this problem, we plan to use a cluster of triangular shape nanoantennas, designed so that the excitation of surface plasmon waves concentrates light at the tip of the nanoantennas. In order to maintain a unidirectional flow of the THz photocurrent along the nanoantennas, a dielectric insulator layer will be placed between the nanoantenna metal and substrate everywhere, except at the tip of the

nanoantennas, to limit the photocurrent injection to the tips. This is expected to greatly enhance the optical-to-THz conversion efficiency.

The second limitation of the first-generation bias-free photoconductive THz source is that a large fraction of the injected photocurrent to the nanoantennas leak to the substrate due to the very high conductivity of the highly-p-type doped substrate. In order to reduce this leakage current, we plan to etch away the InAs layers that are not under the triangular nanoantennas to increase the impedance seen from the nanoantenna tips toward the substrate. This will subsequently increase the THz current driving the nanoantennas and eventually enhance the radiated THz power.

In addition, the triangular nanoantennas will be placed in an array specifically designed to maximize the radiated THz power, while maintaining a healthy radiation pattern.

The design and operation details of the second-generation bias-free photoconductive THz source based on a triangular nanoantenna array are given in Chapter 2.

Chapter 2: Nanoantenna array design

2.1 Nanoantenna array design parameters

In order to enhance the efficiency of the first-generation bias-free photoconductive THz source, a new design has been proposed. The new design is comprised of a triangular nanoantenna array with an overall size of $1mm \times 1mm$. The nanoantenna array is designed to be implemented on the same InAs layers grown on an SI-GaAs substrate used for the first-generation design, which was optimized to provide a large built-in electric field [21]. The nanoantenna array is designed to be surrounded by a silicon nitride anti-reflection layer.

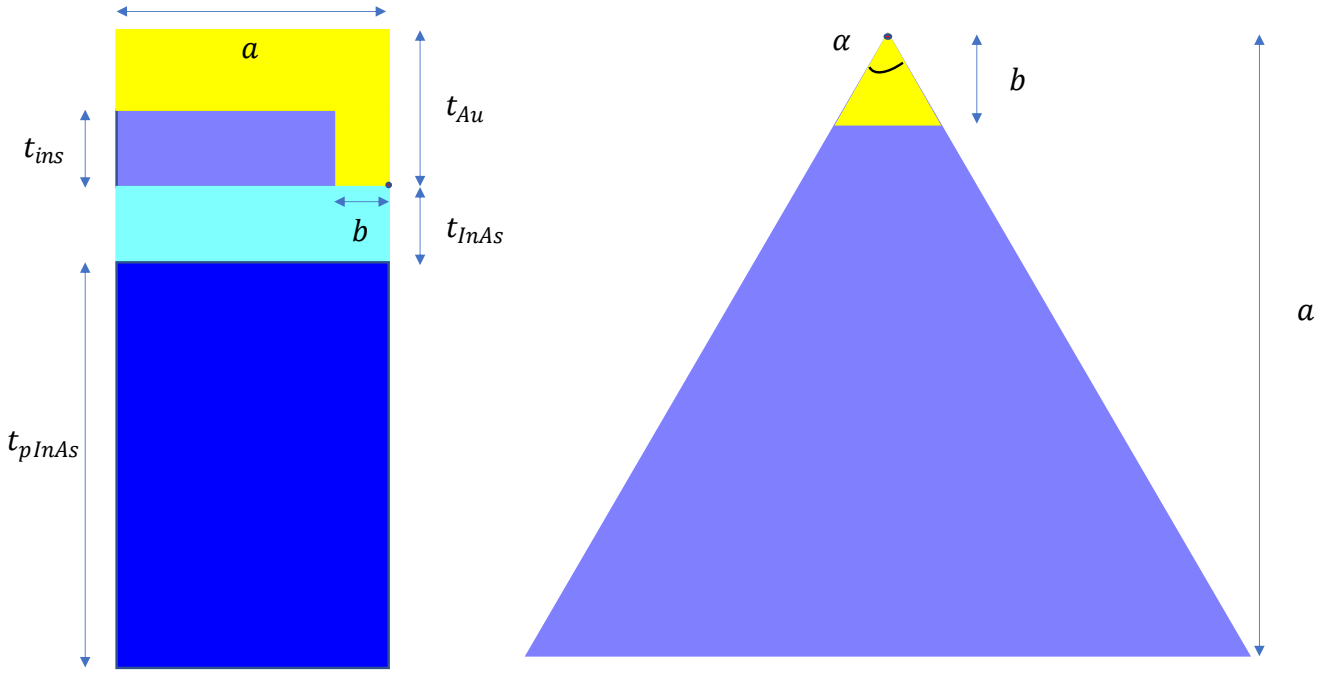

Figure 2.1: Geometric parameters of a triangular nanoantenna element

As shown in Figure 2.1, each nanoantenna is composed of a triangular Ti/Au layer (yellow) which is placed over the InAs layers (light and dark blue) with a sapphire insulating dielectric layer (lilac) in between to minimize the leakage of current from the nanoantenna to the substrate.

The size of the nanoantenna is described by the parameter a, which is the perpendicular distance between the tip and the base of the triangular layer. The angle of the triangular nanoantenna is given by α.

The height of the Ti/Au layer, which is dominated by the Au thickness, is given by t_{Au}. The quantity b describes the region where there is no dielectric layer, and the Ti/Au layer is directly in contact with the undoped InAs layer.

The sapphire insulator layer with a height t_{ins} is deposited over the undoped InAs layer. The height of the undoped InAs layer is given by t_{InAs} and is fixed to 100 nm. The height of the p^+ doped InAs layer is given by t_{pInAs} and is fixed to 500 nm.

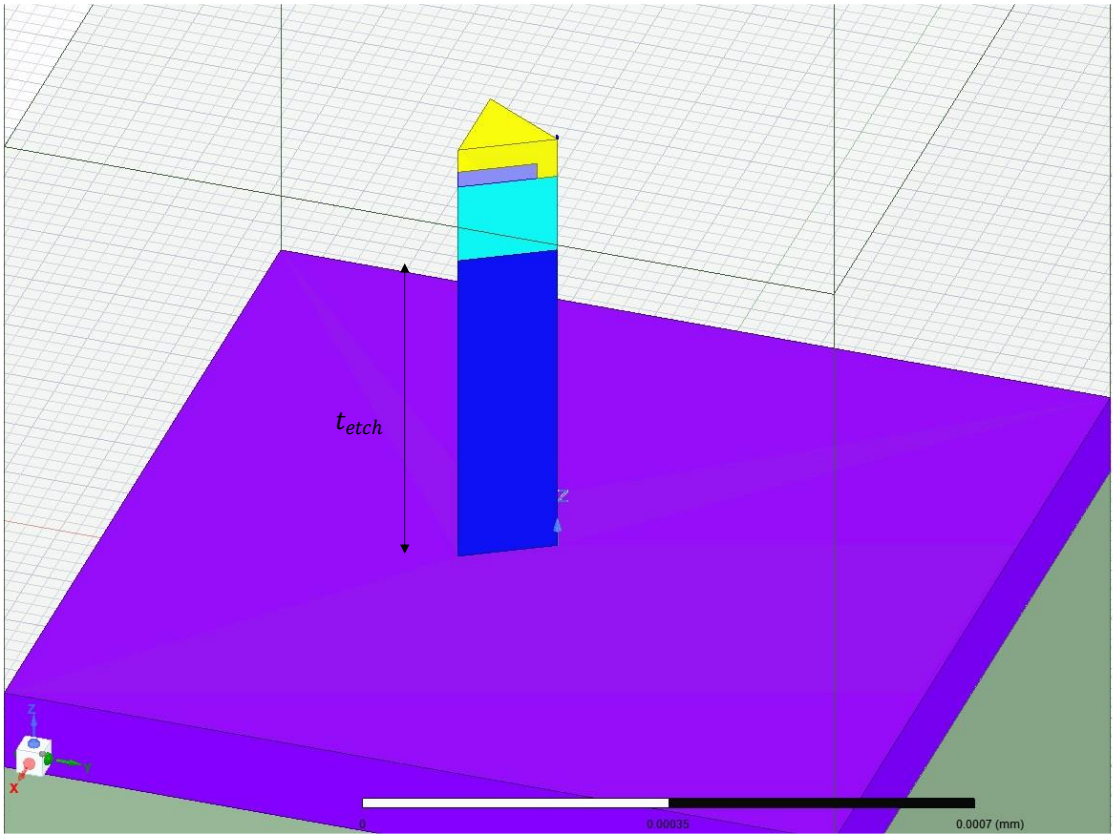

Figure 2.2: Schematic of a single nanoantenna with the p^+ doped InAs layer being partially etched. The unetched section of the p^+ doped InAs is shown in purple.

In order to minimize current leakage from the nanoantenna to the substrate we etch away the InAs layers outside the nanoantenna region to increase the impedance seen from the tip of the nanoantenna toward the substrate. We completely etch away the undoped InAs layer. We assign a parameter t_{etch} which is the height of the p^+ doped InAs that is etched away as shown in Figure 2.2. This parameter can range from 0 (p^+ doped InAs not etched) to 500 nm (p^+ doped InAs completely etched). The periodicity of the nanoantenna array in the x and y directions are given by p_x and p_y, respectively, as shown in Figure 2.3.

2.2 Circuit model of the nanoantenna array

In order to investigate the impact of different geometric parameters on the performance of the nanoantenna array, we extract the equivalent circuit model of the nanoantenna array, as shown in Figure 2.3.

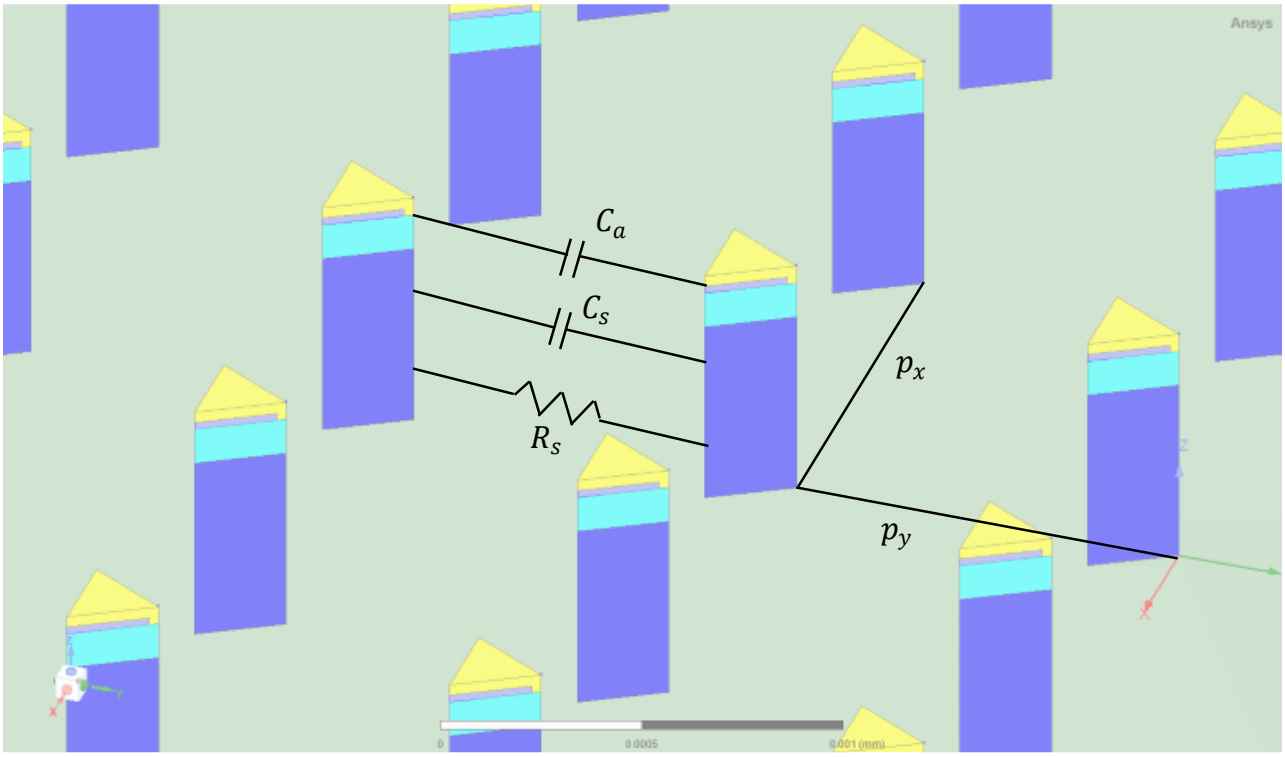

Figure 2.3: The nanoantenna array is modeled as a parallel RC circuit with an antenna capacitance (C_a), a substrate capacitance (C_s) and a substrate resistance (R_s). The periodicity of the nanoantenna array in the x and y directions are given by p_x and p_y, respectively.

Since each nanoantenna is of a length scale much smaller than the wavelength, it can be modeled as a capacitor. Its capacitance is comprised of the capacitance of the individual nanoantenna as well as the mutual capacitance with the adjacent nanoantennas and the substrate. The self-capacitance of the nanoantenna, which is proportional to the inverse square of the length

of the nanoantenna, is much smaller than the mutual capacitance with the adjacent nanoantennas and the substrate.

The mutual capacitance of the nanoantenna with the adjacent nanoantennas is modeled as a parallel plate capacitance. The size of the nanoantenna is directly proportional to the area of this parallel plate capacitor. The periodicity of the array is directly proportional to the distance between the parallel plates in this model.

It is important to note that when the p^+ doped InAs layer is not completely etched away, it behaves as a highly conductive layer modeled by an image nanoantenna. The resulting image capacitance can also be modeled as a parallel plate where the size of the nanoantenna is the area of the plates and the distance between the two plates is given by $2(t_{InAs} + t_{etch})$. We denote the total nanoantenna capacitance with the parameter C_a.

As mentioned before, the substrate is modeled as a parallel RC circuit. The resistance of the substrate is denoted by R_s and can be modeled by the resistance of the path of current flowing from a given nanoantenna to its closest neighboring nanoantennas. In case of incomplete etching, this R_s will be quite low since the InAs layers have very low resistivity. When we completely etch the p^+ doped InAs region, R_s will be very large, dominated by the resistance of the SI-GaAs substrate, which has a very high resistivity. In this case we can approximate $R_S \to \infty$.

The capacitance of the substrate is denoted by C_s and is comprised of the capacitances between the InAs pillars. These capacitances can also be modeled as parallel plates just like the mutual capacitance of the nanoantenna.

We assign the terms Z_a and Z_s to the impedances seen from the tip of the nanoantenna toward the nanoantenna and substrate, respectively. For a 1A input photocurrent injected to the nanoantenna tip, the leakage current can be given by,

$$I_{leak} = \frac{Z_a}{Z_s + Z_a} = \frac{\frac{1}{j\omega C_a}}{\frac{R_s \times \frac{1}{j\omega C_s}}{R_s + \frac{1}{j\omega C_s}} + \frac{1}{j\omega C_a}} \tag{2.1}$$

In order to minimize the leakage current to the substrate, the quantity $\frac{Z_s}{Z_a}$ needs to be maximized. In other words, the substrate impedance should be as high as possible, while having a low nanoantenna impedance by increasing the nanoantenna capacitance as much as possible. Chapter 3 describes the optimization process that not only minimizes the leakage current but also ensures a high optical absorption and high radiation efficiency to further enhance the optical-to-THz conversion efficiency.

Chapter 3: Design optimization

3.1 Design optimization strategy

The total radiated power by the nanoantenna array can be theoretically given by,

$$P_{rad} = AF \times (I_{ant})^2 R_{rad} \tag{3.1}$$

Here AF is the antenna array factor, I_{ant} is the THz current driving each nanoantenna, and R_{rad} is the THz radiation resistance of a single nanoantenna.

If we consider that the optical power incident on the nanoantenna array is given by P_0. The total power incident on each nanoantenna unit is given by,

$$P_{inc} = P_0 \times \frac{p_x p_y}{10^{-6}} \tag{3.2}$$

Here the terms p_x and p_y are the periodicities of the array in the *x* and *y* directions and the denominator is the total area of the array which is $1mm \times 1mm$.

If we consider the power absorbed in the undoped InAs region below the nanoantenna contact with this layer for each unit cell to be P_{abs}, we can write the expression for the current driving each nanoantenna as,

$$I_{ant} = \eta_0 \frac{q}{E_{ph}} (1 - \eta_l) P_{abs} \tag{3.3}$$

In this case, η_0 is the fraction of the photo-generated electrons in the undoped InAs layer drifting to the nanoantenna, q is the electron charge, and E_{ph} is the photon energy. The term η_l is the

proportion of the current that leaks to the substrate. This quantity depends on the geometry of the nanoantenna and is closely tied to the contact area of the nanoantenna metal and the undoped InAs layer (denoted by the length b).

The total optical-to-THz conversion efficiency of the designed nanoantenna array can be given by,

$$\eta_{tot} = \frac{P_{rad}}{P_0} = \frac{AF(I_{ant})^2 R_{rad}}{P_0} \tag{3.4}$$

In order to maximize the total radiated power and efficiency, it is important to maintain high optical absorption (P_{abs}), while minimizing the fraction of the THz leakage current from the nanoantenna back into the substrate (η_l). It is also important to make sure that the radiation resistance of the nanoantenna is high in order to maximize the radiated power.

The next section covers the THz simulations of the nanoantennas that are performed to estimate the fraction of the THz current leaked from each nanoantenna to the substrate as a function of various crucial geometric parameters.

Following that, the optical simulations of the nanoantennas are detailed. These simulations provide the estimated absorbed power fraction of a 1550 nm optical pump beam incident on the nanoantenna array and, subsequently, the number of the photo-generated carriers that are injected to the nanoantennas.

Finally, a simple Hertzian dipole model for the nanoantenna radiation resistance at THz frequencies is used and the impact of the array periodicity on the array factor is studied. The overall optimization involves maximizing P_{rad} and η_{tot} taking the optical absorption, THz leakage

current, nanoantenna radiation resistance and array factor into consideration, for various nanoantenna geometries.

3.2 THz Simulations

The nanoantenna model was set up in the ANSYS HFSS [22] design environment. The structure was excited using a 1A current source under periodic boundary conditions. The leakage current was calculated in MATLAB [23] using the extracted data for the current density and the electric field below the interface of the nanoantenna metal and the undoped InAs layer.

With this procedure, the variation of the leakage current as a function of various physical design parameters have been obtained, which was used to find the optimal geometric parameters to minimize the leakage of current to the substrate.

3.3 Material properties at THz frequencies

The electric properties of Au at THz frequencies [24] suggest that it is a very good conductor even at these frequencies. For this study, the Drude model values of the bulk conductivity of Au (approximately $4 \times 10^7 S/m$) have been used. The electric properties of Sapphire at THz frequencies were obtained from previously reported experimental measurements [25]. The dielectric properties of the undoped and p^+ doped InAs were calculated using the Drude model [26]. The undoped InAs layer is expected to have varying properties as a function of the depth in the InAs layer due to the sharp band bending in this layer, as shown in Figure 3.1.

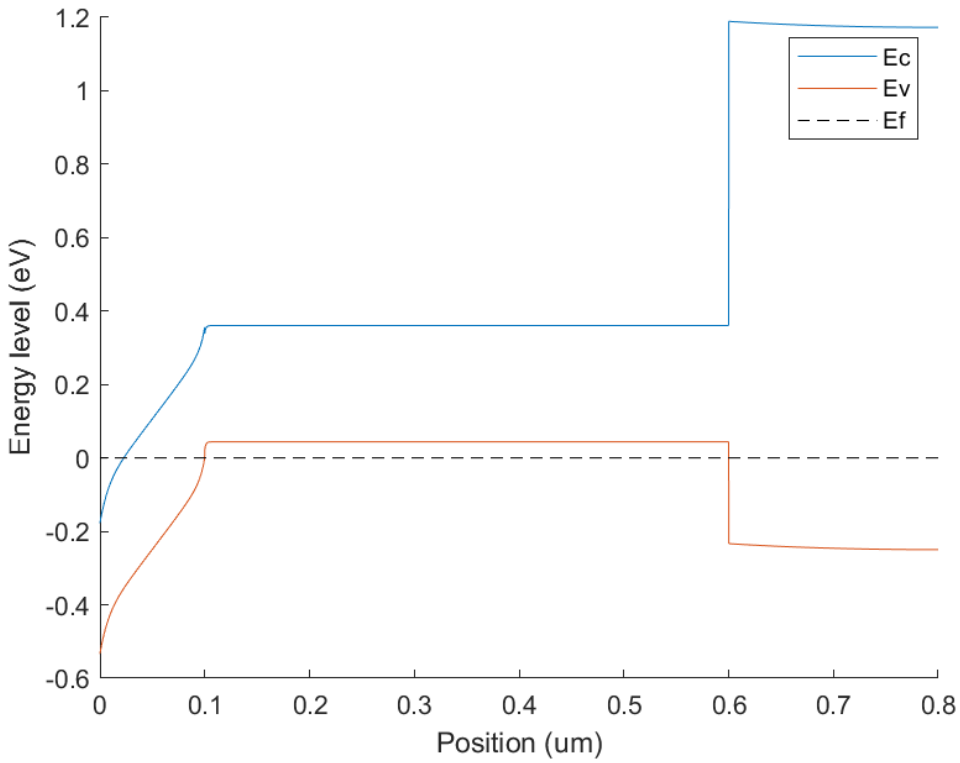

Figure 3.1: The band structure of the undoped InAs layer (0-0.1um) followed by the p^+ doped InAs layer (0.1-0.6 um) and the SI-GaAs substrate (0.6-0.8 um).

In order to simplify the optimization procedure, we choose a worst-case scenario in terms of the conductivity ($10^6 S/m$) for the undoped InAs layer when calculating the leakage current. This conductivity corresponds to the highest possible conductivity in the undoped InAs layer in the presence of band-bending. The leakage current of the real device will be much lower than this value since there will be lower conductivity regions within the undoped InAs layer.

3.4 THz leakage current simulations

In order to minimize the leakage current and optimize device performance, the variation of the leakage current as a function of various geometric parameters have been simulated and analyzed using the introduced circuit model.

3.4.1. The impact of the etch height

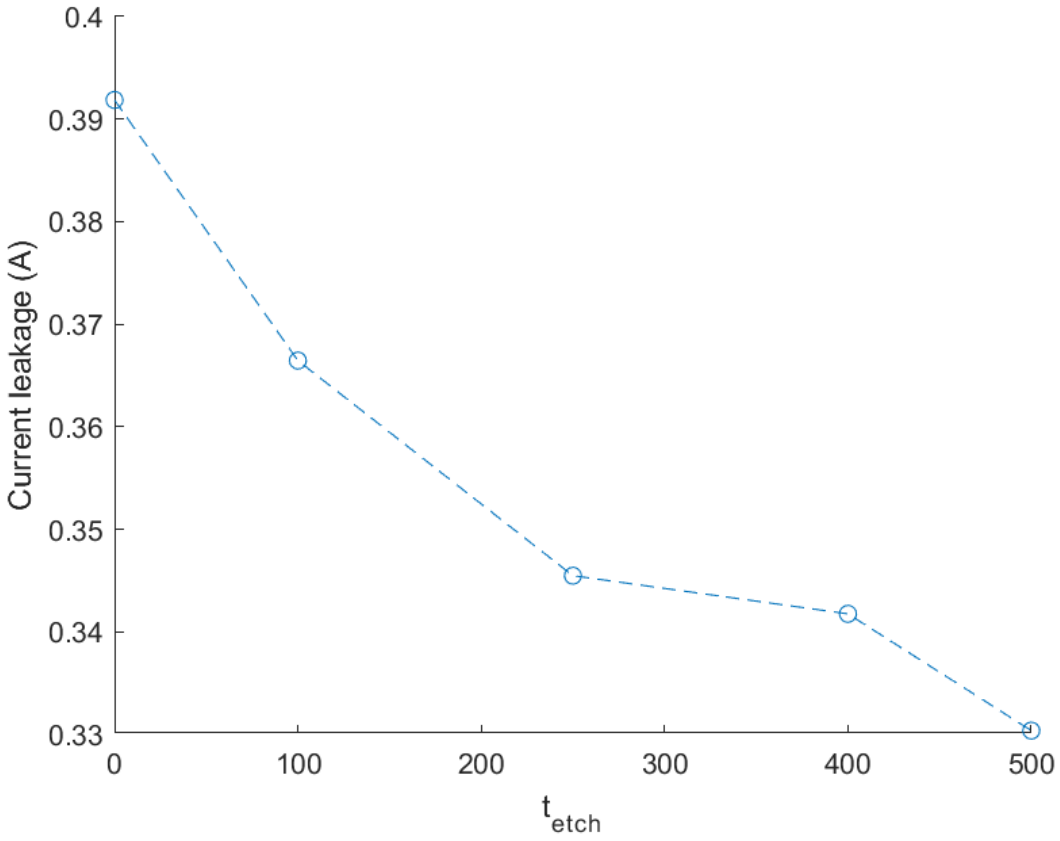

Figure 3.2: Variation of the THz leakage current with t_{etch}

Simulation results shown in Figure 3.2 show that the current leaking to the substrate reduces as we increase t_{etch}. This can be explained using the circuit model because C_a increases due to an increased mutual capacitance. This causes Z_a to decrease. Also, R_s increases as we etch deeper since we reduce the area of the current flow path. Eventually, when we completely etch the p^+ doped layer, we have a very high R_s. This increases the substrate impedance.

3.4.2. The impact of periodicity

Simulation results in Figure 3.3 show that the THz leakage current decreases when decreasing the periodicity of the nanoantenna. According to the circuit model, as the periodicity of the

nanoantenna array decreases, the distance between the parallel plates in the capacitor model decreases which increase the quantity C_a. Thus, Z_a and subsequently I_{leak} decrease. While there is also a decrease in C_s, the overall change in Z_s is not as much as the change in Z_a due to the presence of R_s.

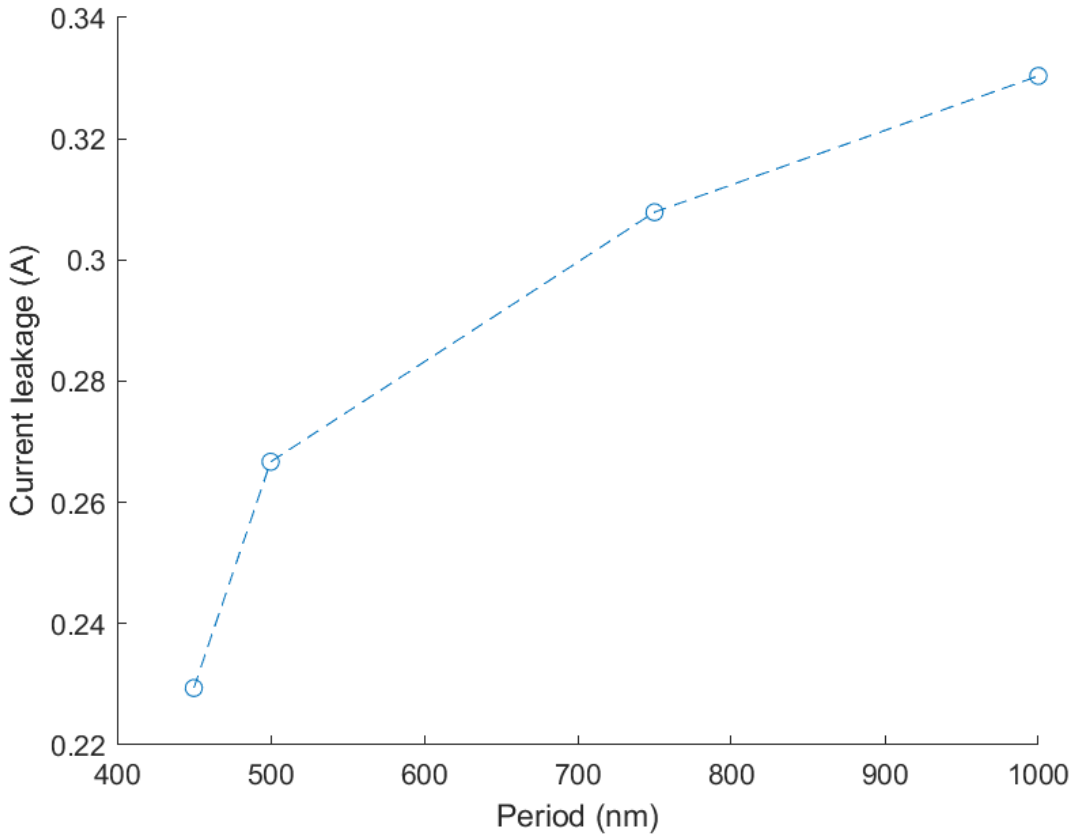

Figure 3.3: Variation of the THz leakage current with the periodicity of the nanoantenna

It should be noted that when we decrease p_y , I_{leak} reduces more rapidly than when we decrease p_x by the same amount, as seen in Figure 3.4. This implies that the y direction mutual capacitance is more dominant in the overall mutual capacitance.

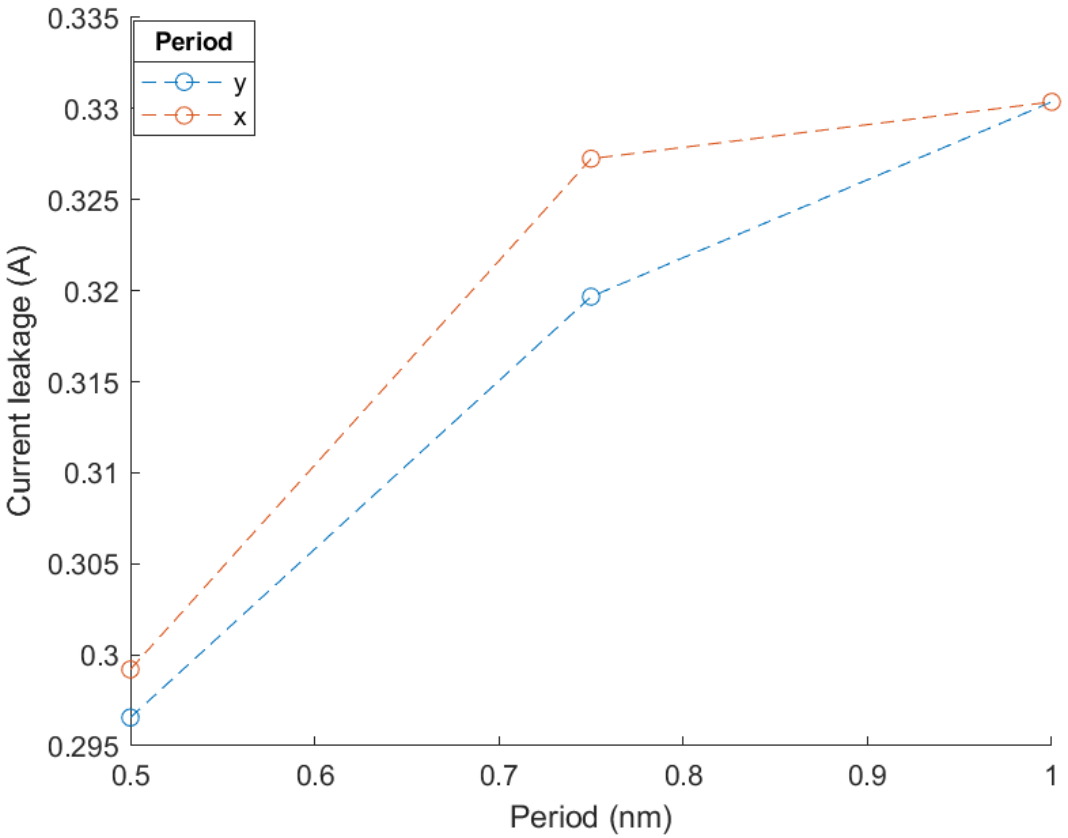

Figure 3.4: The variation of the THz leakage current when changing only p_y or p_x, while keeping the other periodicity fixed at 1000 nm.

3.4.3. The impact of frequency

The impedance of the capacitive components is scaled down with an increase in frequency. However, there is no such scaling for the resistive elements. Thus, Z_a will decrease much more than Z_s with an increase in the frequency. This implies that leakage current will be greatly reduced with an increase in frequency, as seen in Figure 3.5.

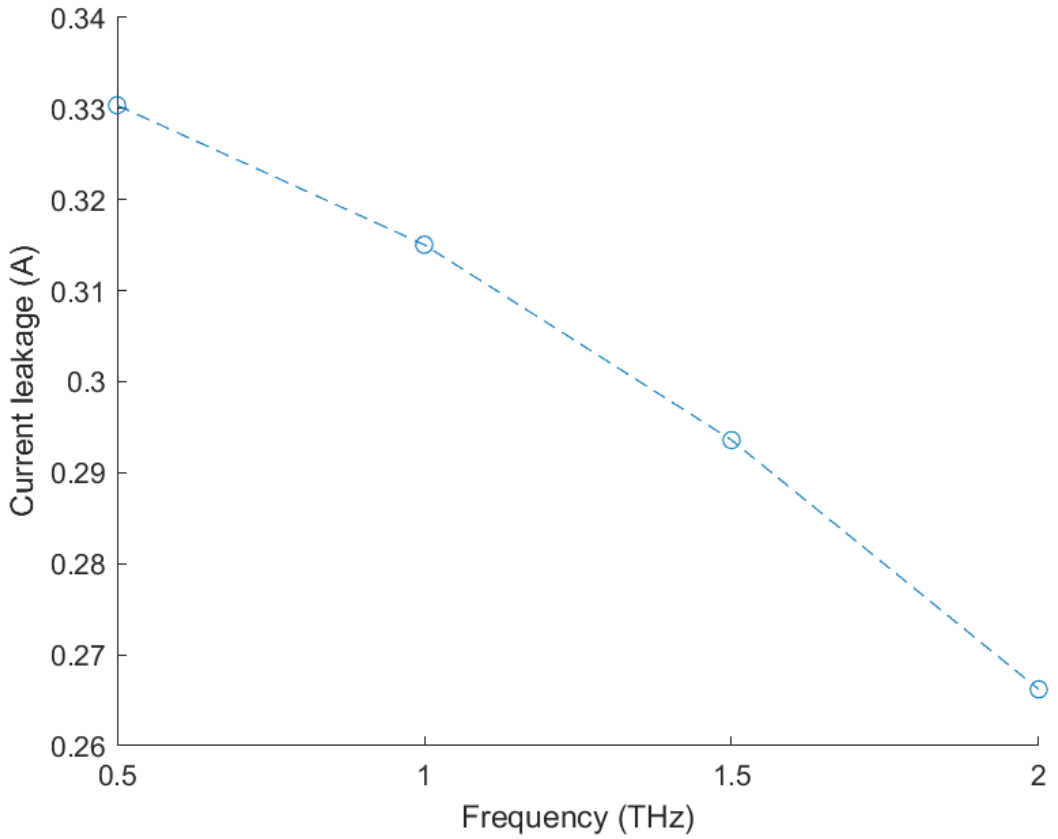

Figure 3.5: Variation of the THz leakage current as a function of the operation frequency.

3.4.4. The impact of the nanoantenna size

Figure 3.6 shows that there is a decrease in the THz leakage current when increasing the size of the nanoantenna, a. According to the circuit model, increasing the size of the nanoantenna can change the value of C_a in two different ways.

Increasing the size of the nanoantenna reduces the self-capacitance but the mutual capacitance with the nearby nanoantennas increases since the area of the parallel plate capacitors increase. Since the self-capacitance is much smaller in magnitude than the mutual capacitance, the mutual capacitance dominates and the C_a value increases. This increase in C_a results in a decrease in the leakage current when we increase the nanoantenna size, a.

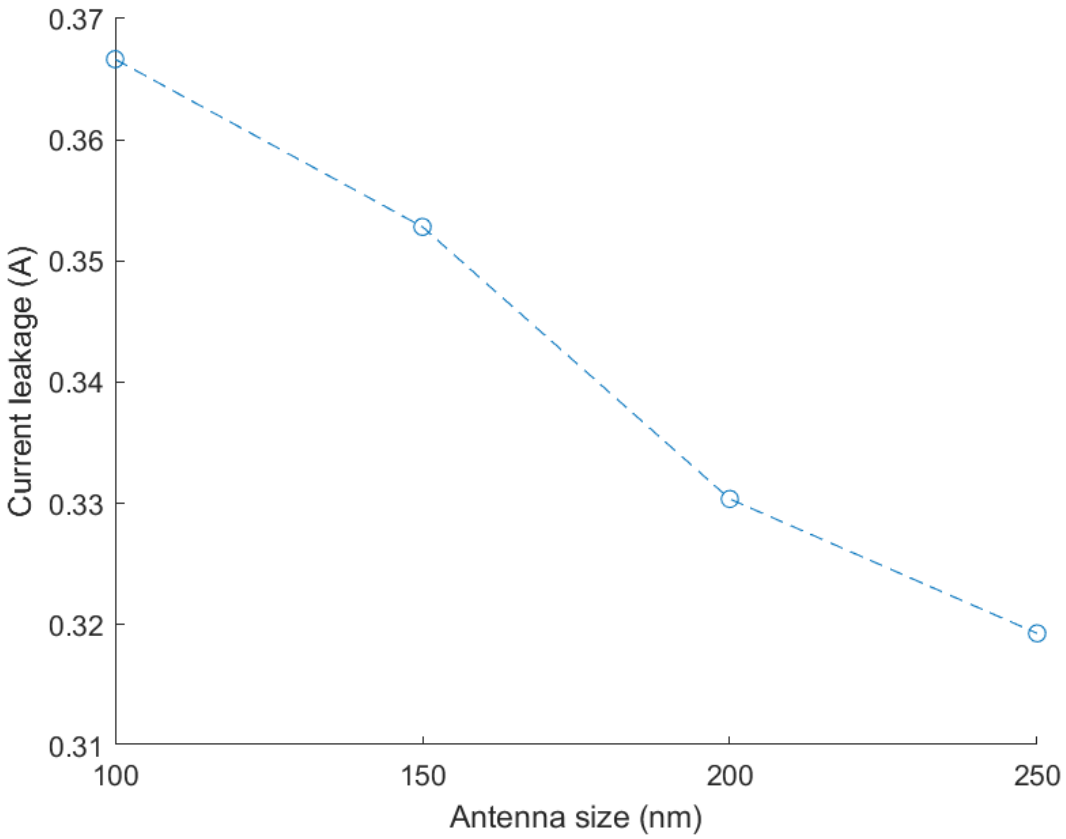

Figure 3.6: Variation of the THz leakage current as a function of the nanoantenna size, a.

3.4.5. The impact of the nanoantenna contact area with the substrate

As seen in Figure 3.7, increasing the nanoantenna contact area with the undoped InAs layer results in a decrease in the THz leakage current. With an increase in the exposed area, the effective area of the nanoantenna is increased since it is connected to the undoped InAs substrate, which can be considered as a good conductor. This causes a slight increase in C_a which causes a slight decrease in the leakage current.

It is important to note that the nanoantenna contact area with the undoped InAs layer (the geometric parameter *b*) has a bigger impact on the absorbed optical power in the undoped InAs layer under the nanoantenna contact (P_{abs}) and, thus, the THz current driving the nanoantenna

(I_{ant}). A larger size of b would result in higher current input to the nanoantenna from the substrate. This is reflected in the formula for the total radiated power in Sec 3.1

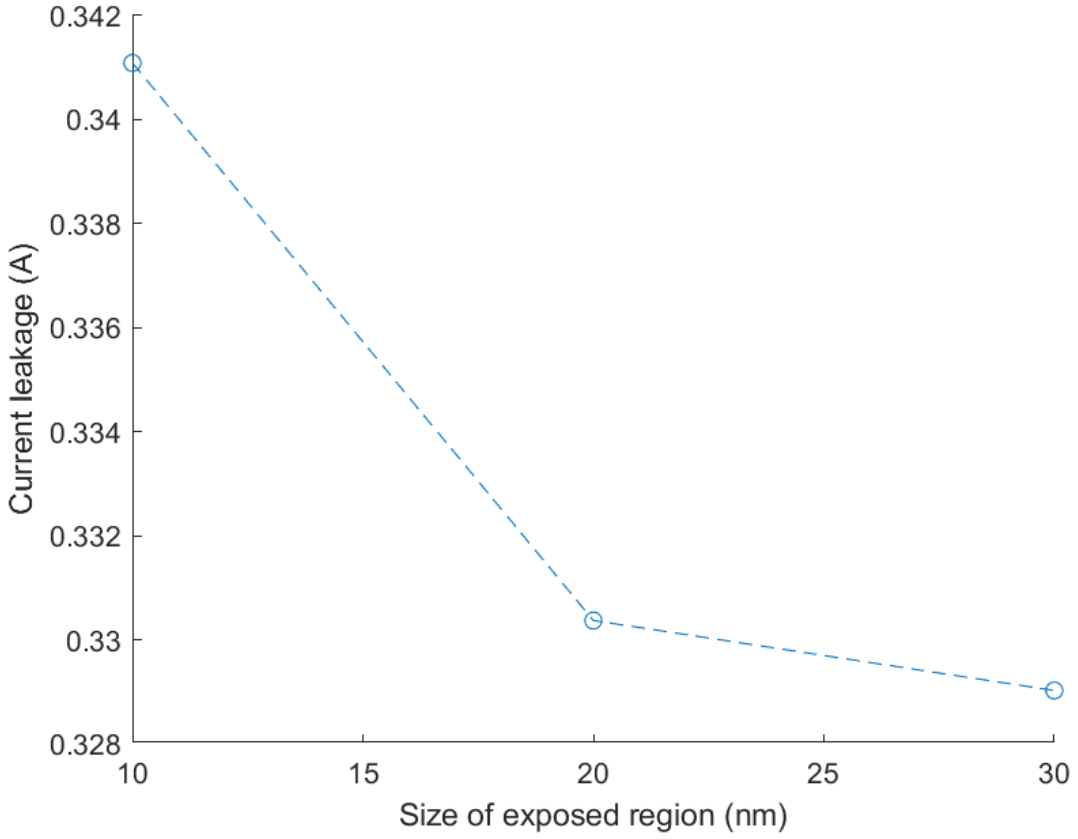

Figure 3.7: Variation of the THz leakage current as a function of the nanoantenna contact area with the undoped InAs layer, b.

3.4.6. The impact of the nanoantenna triangular angle

With an increase in the nanoantenna triangular angle, α, the size of the nanoantenna increases. This results in an increase in the area of the face of the parallel plate in the model for the nanoantenna capacitance. Thus, C_a increases, resulting in a decrease in Z_a and subsequently I_{leak}. The parameter α seems to be the most impactful geometric parameter in reducing the leakage current (40% to 20% drop in leakage) as seen in Figure 3.8.

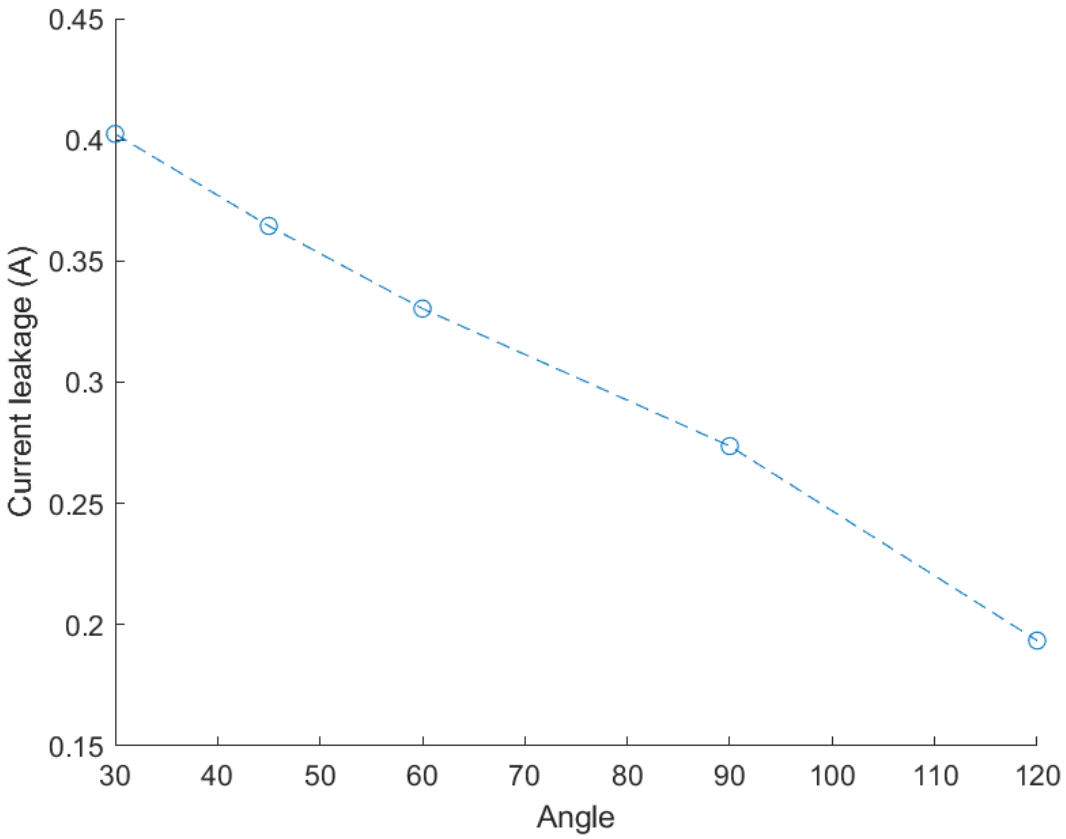

Figure 3.8: Variation of the THz leakage current as a function of the nanoantenna triangular angle.

In summary, in order to minimize the leakage current, it is important to have a large nanoantenna with a large angle and as small a period as possible. However, the optimization of the nanoantenna for maximum power and efficiency depends on the optical performance and radiation efficiencies as well, which are discussed in the following sections.

3.5 Optical simulations

The presented device structure was also simulated in the optical frequency domain in order to identify optimized geometric parameters to maximize the absorption of the 1550 nm light in the

undoped InAs layer under the nanoantenna contact (P_{abs}) and, thus, the THz current driving the nanoantenna.

The simulation was performed in a COMSOL Multiphysics solver [27]. The nanoantenna structure was set up under periodic boundary conditions in the x and y directions with a perfectly matched layer (PML) at the top and bottom to absorb the reflected and transmitted light to prevent multiple reflection of the EM wave at the boundary. The structure was excited using a 1550 nm electromagnetic wave that was incident normally on the structure with its electric field polarized along the length of the triangular nanoantenna (a). By integrating the optical absorption over the volume of the undoped InAs that is directly under the nanoantenna metal, the optical absorption P_{abs} was calculated.

3.6 Optical absorption optimization

In order to optimize the nanoantenna geometry for maximum optical power absorption, we performed simulations with various geometric parameters.

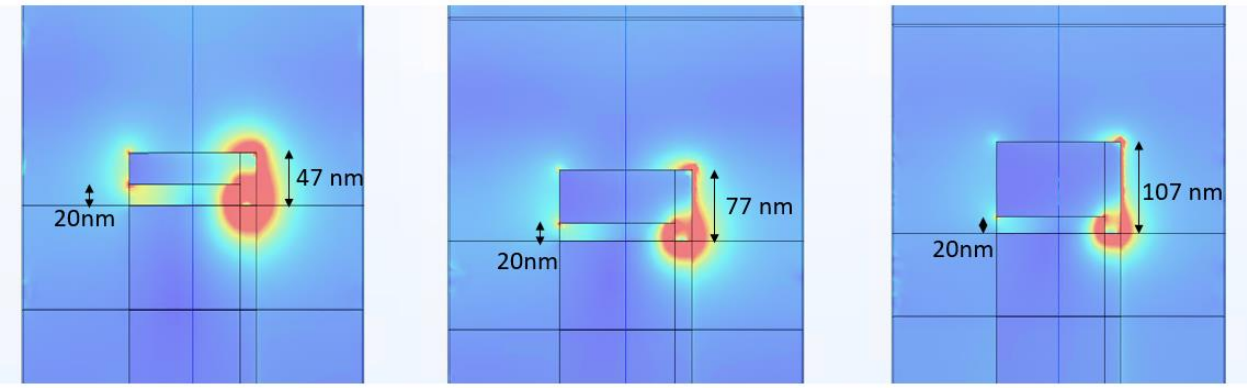

Figure 3.9: Optical absorption profile for three different metal thicknesses, t_{Au}, while t_{ins} is fixed at 20 nm.

The anti-reflection coating material was chosen by analyzing the absorption of light for different refractive indices of the anti-reflection coating. Silicon nitride was eventually chosen because of its superior absorption characteristics. It was found through multiple simulations that the thickness of the metal above the insulator layer ($t_{Au} - t_{ins}$) should be greater than the thickness of the insulator layer (t_{ins}). This is because we want the excitation mode to be restricted to the undoped InAs region rather than the anti-reflection coating. At the same time, t_{Au} should be as small as possible to increase the optical coupling to the undoped InAs region under the nanoantenna metal, as shown in Figure 3.9.

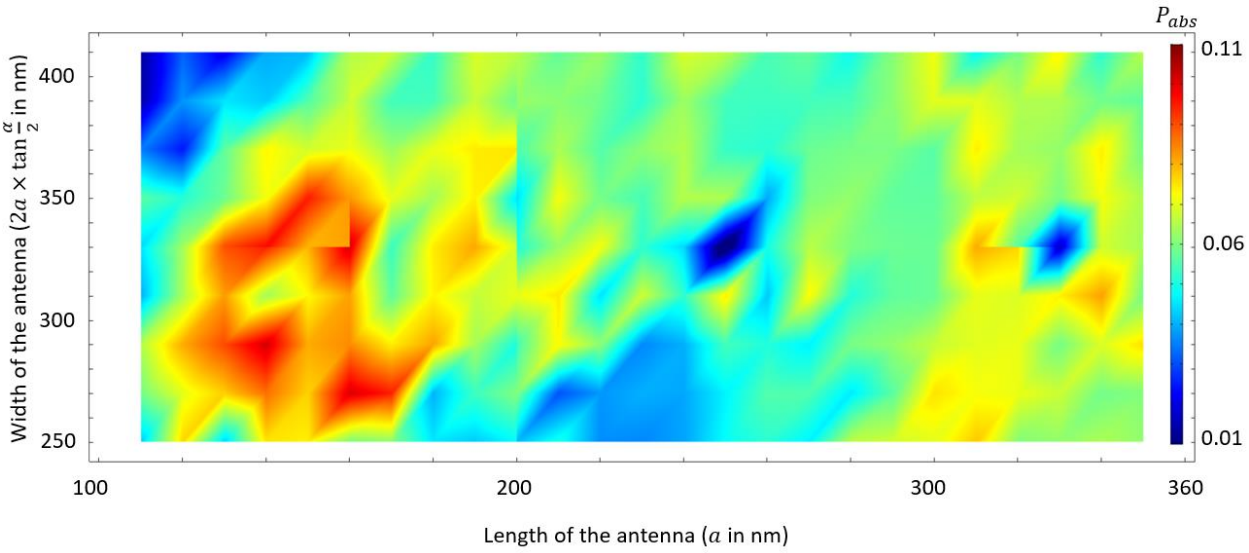

Figure 3.10: The absorption of a 1550 nm optical beam in the undoped InAs layer under the nanoantenna contact (P_{abs}) as a function of the nanoantenna dimensions for a 500 nm periodicity in the x and y directions.

As seen in Figure 3.10, a large geometric sweep was conducted to identify the nanoantenna geometries that maximize optical absorption. While multiple local absorption peaks are observed for a 1550 nm incident light, the THz performance at all these points must be considered (described in section 3.1) in order to find the best point of operation for the device.

3.7 Nanoantenna radiation resistance

Since the length scale of each individual nanoantenna is much smaller than THz wavelengths, we can model each individual nanoantenna as a Hertzian dipole antenna [28]. The radiation resistance of each nanoantenna is thus given by,

$$R_{rad} = 80\pi^2 \left(\frac{l}{\lambda}\right)^2 \tag{3.5}$$

In this case, l is the length of the antenna and λ is the operation wavelength. In case of the triangular nanoantenna, as a first order of approximation, we have used the length of the nanoantenna, *a*, in the formula above.

3.8 Antenna array factor

Since we know the radiation pattern of a single nanoantenna, we multiply it with the array factor in order to get the total radiation power and radiation pattern of the array. The array factor of a planar array [28] is given by,

$$AF(\theta, \phi) = \frac{\sin\left(\frac{M}{2}\psi_x\right)}{\sin\left(\frac{\psi_x}{2}\right)} \times \frac{\sin\left(\frac{N}{2}\psi_y\right)}{\sin\left(\frac{\psi_y}{2}\right)} \tag{3.6}$$

In this case, M and N are the numbers of the antennas in a single row in the x and y directions, respectively. This array factor is not normalized for the total number of the nanoantennas in the array.

Since the designed nanoantenna array has a $1mm \times 1mm$ area, we can obtain M and N as

$$M = \frac{10^{-3}}{p_x} \tag{3.7}$$

$$N = \frac{10^{-3}}{p_y} \tag{3.8}$$

We also have,

$$\psi_x = kp_x \sin\theta \cos\phi \tag{3.9}$$

$$\psi_y = kp_y \sin\theta \sin\phi \tag{3.10}$$

It is important to note that the term k which refers to the wavenumber has a discontinuity at $\theta = \frac{\pi}{2}$ because there is a change in the medium from air to the SI-GaAs substrate. We use this array factor and multiply it with the electric field of a single nanoantenna to obtain the total radiated power and the radiation pattern of the array.

3.9 Optimum design

After detailed optical and THz simulations and investigating the impact of various geometric parameters of the nanoantenna array on the optical and THz characteristics of the device, we

identified the design that offers the maximum radiated power and efficiency, with the following geometric parameters:

Table 1: Design parameters of the optimized nanoantenna array structure

Geometric parameter	Value
a	310 nm
α	$\frac{\pi}{3}\ rad$
b	20 nm
t_{ins}	20 nm
t_{Au}	50 nm
t_{InAs}	100 nm
t_{pInAs}	500 nm
t_{etch}	400 nm
p_x	500 nm
p_y	500 nm

While these parameters may not provide the maxima of the optical absorption or the minima of the THz leakage current, they have been chosen to maximize the overall radiated power and efficiency of the nanoantenna array.

Chapter 4: Conclusions and Future Work

This new generation of bias-free photoconductive sources designed for optical-to-THz conversion is expected to provide a significant enhancement in the radiated power and efficiency due to lower THz leakage current, unidirectional current flow along the nanoantennas, and higher radiation resistance levels. Specifically, this new design offers several improvements over the previous generation of bias-free sources by reducing the THz leakage current from over 90% to under 20%. This leakage current reduction was achieved by etching the high-conductivity InAs layer around the nanoantennas and by including a sapphire insulator layer between the nanoantenna metal and undoped InAs layer, except at the nanoantenna tip.

Since the THz photocurrent is injected from the substrate to the tip of the triangular nanoantenna, there is a unidirectional flow of the current instead of the standing waves that were detrimental to the radiation performance of the first-generation bias-free photoconductive sources. The smaller size of the nanoantenna unit cell also helps to increase the fill factor of the array.

In the next steps, the optimized devices will be fabricated and characterized under both pulsed and continuous wave (CW) operation. Characterization of the radiation pattern and the radiated power of the array will be performed, and the results will be compared with the theoretical predictions. We also plan to explore alternative orientations and shapes of nanoantennas in order to manipulate the spatial, spectral, and polarization characteristics of the generated THz radiation.

References

1. Charrada, K., Zissis, G., & Aubes, M. (1996). Two-temperature, two-dimensional fluid modelling of mercury plasma in high-pressure lamps. Journal of Physics D: Applied Physics, 29(9), 2432–2438. https://doi.org/10.1088/0022-3727/29/9/030
2. Bonner, L. G. (1937). A new type globar support for infrared spectrometry. Review of Scientific Instruments, 8(7), 264–265. https://doi.org/10.1063/1.1752308
3. Levialdi, A., & Darrow, K. K. (1940). On a scheme for mounting ``globar" for researches in the infra-red. Review of Scientific Instruments, 11(12), 429–429. https://doi.org/10.1063/1.1751602
4. Lewen, F., Michael, E., Gendriesch, R., Stutzki, J., & Winnewisser, G. (1997). Terahertz laser sideband spectroscopy with backward wave oscillators. Journal of Molecular Spectroscopy, 183(1), 207–209. https://doi.org/10.1006/jmsp.1996.7244
5. Dobroiu, A., Yamashita, M., Ohshima, Y. N., Morita, Y., Otani, C., & Kawase, K. (2004). Terahertz imaging system based on a backward-wave oscillator. Applied Optics, 43(30), 5637. https://doi.org/10.1364/ao.43.005637
6. Bhattacharjee, S., Booske, J. H., Kory, C. L., van der Weide, D. W., Limbach, S., Gallagher, S., Welter, J. D., Lopez, M. R., Gilgenbach, R. M., Ives, R. L., Read, M. E., Divan, R., & Mancini, D. C. (2004). Folded waveguide traveling-wave tube sources for terahertz radiation. IEEE Transactions on Plasma Science, 32(3), 1002–1014. https://doi.org/10.1109/tps.2004.828886

7. Idehara, T., Saito, T., Ogawa, I., Mitsudo, S., Tatematsu, Y., La Agusu, Mori, H., & Kobayashi, S. (2008). Development of terahertz fu CW gyrotron series for DNP. Applied Magnetic Resonance, 34(3-4), 265–275. https://doi.org/10.1007/s00723-008-0132-6
8. Byrd, J. M., Leemans, W. P., Loftsdottir, A., Marcelis, B., Martin, M. C., McKinney, W. R., Sannibale, F., Scarvie, T., & Steier, C. (2002). Observation of broadband self-amplified spontaneous coherent terahertz synchrotron radiation in a storage ring. Physical Review Letters, 89(22). https://doi.org/10.1103/physrevlett.89.224801
9. Williams, G. P. (2003). High–power terahertz synchrotron sources. Philosophical Transactions of the Royal Society of London. Series A: Mathematical, Physical and Engineering Sciences, 362(1815), 403–414. https://doi.org/10.1098/rsta.2003.1325
10. Dem'yanenko, M. A., Esaev, D. G., Knyazev, B. A., Kulipanov, G. N., & Vinokurov, N. A. (2008). Imaging with a 90frames⁄s microbolometer focal plane array and high-power terahertz free electron laser. Applied Physics Letters, 92(13), 131116. https://doi.org/10.1063/1.2898138
11. Zvyagin, S. A., Ozerov, M., Čižmár, E., Kamenskyi, D., Zherlitsyn, S., Herrmannsdörfer, T., Wosnitza, J., Wünsch, R., & Seidel, W. (2009). Terahertz-range free-electron laser electron spin resonance spectroscopy: Techniques and applications in high magnetic fields. Review of Scientific Instruments, 80(7), 073102. https://doi.org/10.1063/1.3155509
12. Yang, L., Long, S., Guo, X., & Hao, Y. (2012). A comparative investigation on sub-micrometer inn and Gan Gunn diodes working at Terahertz Frequency. Journal of Applied Physics, 111(10), 104514. https://doi.org/10.1063/1.4721667

13. Wang, X., Shen, C., Jiang, T., Zhan, Z., Deng, Q., Li, W., Wu, W., Yang, N., Chu, W., & Duan, S. (2016). High-power terahertz quantum cascade lasers with ∼0.23 W in continuous wave mode. AIP Advances, 6(7), 075210. https://doi.org/10.1063/1.4959195
14. Wang, W., Cong, Z., Chen, X., Zhang, X., Qin, Z., Tang, G., Li, N., Wang, C., & Lu, Q. (2014). Terahertz parametric oscillator based on ktiopo_4 crystal. Optics Letters, 39(13), 3706. https://doi.org/10.1364/ol.39.003706
15. Manley, J., & Rowe, H. (1956). Some general properties of nonlinear elements-part I. General Energy Relations. Proceedings of the IRE, 44(7), 904–913. https://doi.org/10.1109/jrproc.1956.275145
16. Auston, D. H., Cheung, K. P., & Smith, P. R. (1984). Picosecond photoconducting hertzian dipoles. Applied Physics Letters, 45(3), 284–286. https://doi.org/10.1063/1.95174
17. Berry, C. W., Hashemi, M. R., & Jarrahi, M. (2014). Generation of high power pulsed terahertz radiation using a plasmonic photoconductive emitter array with logarithmic spiral antennas. Applied Physics Letters, 104(8), 081122. https://doi.org/10.1063/1.4866807
18. Berry, C. W., Wang, N., Hashemi, M. R., Unlu, M., & Jarrahi, M. (2013). Significant performance enhancement in photoconductive terahertz optoelectronics by incorporating plasmonic contact electrodes. Nature Communications, 4(1). https://doi.org/10.1038/ncomms2638
19. Yardimci, N. T., Yang, S.-H., Berry, C. W., & Jarrahi, M. (2015). High-power terahertz generation using large-area plasmonic photoconductive emitters. IEEE Transactions on Terahertz Science and Technology, 5(2), 223–229. https://doi.org/10.1109/tthz.2015.2395417

20. Yang, S.-H., Hashemi, M. R., Berry, C. W., & Jarrahi, M. (2014). 7.5% optical-to-terahertz conversion efficiency offered by photoconductive emitters with three-dimensional plasmonic contact electrodes. IEEE Transactions on Terahertz Science and Technology, 4(5), 575–581. https://doi.org/10.1109/tthz.2014.2342505
21. Turan, D., Lu, P. K., Yardimci, N. T., Liu, Z., Luo, L., Park, J.-M., Nandi, U., Wang, J., Preu, S., & Jarrahi, M. (2021). Wavelength conversion through plasmon-coupled surface states. Nature Communications, 12(1). https://doi.org/10.1038/s41467-021-24957-1
22. Ansys® Electronics Desktop 2021 R2, ANSYS, Inc.
23. MATLAB, 2021. version 9.11.0.1769968 (R2021b), The MathWorks, Inc., Natick, Massachusetts, United States
24. Liu, S., Hu, J., Zhang, Y., Zheng, Z., Liu, Y., Xu, R., & Xue, Q. (2015). 1 thz micromachined Waveguide Band-Pass Filter. Journal of Infrared, Millimeter, and Terahertz Waves, 37(5), 435–447. https://doi.org/10.1007/s10762-015-0229-6
25. Grischkowsky, D., Keiding, S., van Exter, M., & Fattinger, C. (1990). Far-infrared time-domain spectroscopy with terahertz beams of dielectrics and semiconductors. Journal of the Optical Society of America B, 7(10), 2006. https://doi.org/10.1364/josab.7.002006
26. Kittel, C., McEuen, P. (2019). Introduction to solid state physics. John Wiley & Sons
27. COMSOL Multiphysics® v. 6.0. www.comsol.com. COMSOL AB, Stockholm, Sweden
28. Balanis, C. A. (2005). Antenna theory: Analysis and design. Wiley-Interscience.